Comput Mech (2007) 40:299–312
DOI 10.1007/s00466-006-0100-7

ORIGINAL PAPER

A 3D implicit unstructured-grid finite volume method for structural dynamics

G.H. Xia · Y. Zhao · J.H. Yeo · X. Lv

Received: 3 May 2006 / Accepted: 25 June 2006 / Published online: 18 July 2006

Abstract In this work, a new vertex-based finite volume method (FVM) using unstructured grids and cell-based data structure is proposed for computational analysis of two-and three-dimensional (2D/3D) general structural dynamic problems. The governing equations are spatially discretized by the FVM and an implicit dual time stepping scheme is employed to integrate the equations in time. The proposed method is applied to calculate deformations and dynamics of 2D and 3D cantilevers, as well as simply supported and clamped square plates. Computational results obtained are found to agree well with analytical solutions. It can be a viable alternative to the traditional finite element method (FEM) for structural dynamic calculations. And it can be seamlessly integrated into FVM-based Computational Fluid Dynamics (CFD) solver for simulating fluid-structure interaction (FSI).

Keywords Finite volume method · Unstructured grid · Dual time stepping · Structural dynamics

1 Introduction

The finite element method (FEM) is the most popular tool for computational structural mechanics (CSM), especially for problems involving nonlinear material properties and nonlinear deformations. And traditionally, the finite volume method (FVM) is widely used in computational fluid dynamics (CFD). Both methods make use of governing equations in integral forms. And both methods are weighted residual methods where they only differ with regard to the type of weighting functions used. FV methods may be considered as a particular case of the FE method with non-Galerkin weighting [1]. Unlike the finite element approach, in which the relevant conservation principle and/or equilibrium of forces, are only satisfied in a global sense, the finite volume procedure is conservative from the whole-domain scale down to the cell or control volume level. Their different properties, applications and directions of development have resulted in numerical software tools for CFD and CSM that are different in almost every aspect. This discrepancy has hindered research progresses in the fields of multi-physics and fluid–structure interaction simulation. The current efforts attempt to bridge this gap and develop a structural dynamic solver that is based on the unstructured-grid FV methodology, in order to integrate the structural and fluid solvers seamlessly in future fluid–structure interaction simulation.

FE methods are generally considered to be more accurate for self-joint problems which are typical of CSM. However the essential difference between FE and FV in the numerical discretization of second-order partial differential equations is negligible and for many cases the two methods are equivalent [2]. In recent years, the FV methods have been applied to a number of problems in various aspects of CSM. For example, plate bending analysis has been performed using FV methods by Demirtzic et al. [3], Wheel [4] and Fallah [5]; the solutions of different solid mechanics problems [6,7], stress analysis of elasto-plastic solids by Demirtzic et al. [8], analysis of dynamic solid mechanics [9] and application to fluid-structure interaction by Slone et al. [10] have also been reported in the literature. These works prove

G.H. Xia · Y. Zhao (✉) · J.H. Yeo · X. Lv
School of Mechanical and Aerospace Engineering,
Nanyang Technological University, Nanyang Avenue,
Singapore 639798, Republic of Singapore
e-mail: myzhao@ntu.edu.sg

that for CSM problems the FV methods are competitive with the FE methods in terms of numerical accuracy and computational efficiency. Wheel [11] even showed that the FV method achieves greater accuracy than the FE method for a benchmark problem using a steel elliptic membrane.

The implementations of FV methods for CSM computations can be classified into two categories: the cell-centered approach [3,4,6,8,11] and the cell-vertex one [1,7,9,10,12]. In the cell-vertex approach, the displacement and stress variables are stored at the vertices of the mesh which are themselves enclosed by control volumes formed by the median duals of the mesh; whereas in the cell-centered method the variables are stored at the centroids of cells which are also used as control volumes themselves. Thus the cell-vertex approach needs considerably less computational effort and memory for a given mesh. For instance in the case of three-dimensional tetrahedral meshes, the stress computations can be performed by looping over edges in the cell-vertex scheme, whereas in a cell-centered scheme they are looped over triangular faces. And the cell-vertex approach is better suited to compute stresses, especially when the meshes become highly irregular. One major drawback of the cell-vertex scheme is that the solution quality is poorer than that of the cell-centered scheme on the same mesh. Both FV approaches are locally and globally conservative and have demonstrated superiority over traditional FE methods in terms of accuracy in selected test cases [11].

This paper describes a new cell-vertex FV method using triangular and tetrahedral cells for general 2D and 3D structural dynamic problems. Stresses are calculated in a cell-by-cell manner based on a cell-based data structure and stress distribution is linear within cells, but can be discontinuous across different cells, even within the same control volume. The control volumes are constructed around vertices using the median dual of the mesh. The deformation gradients and stresses are evaluated using Green theorem. Time-accurate solutions are obtained by employing a implicit dual time stepping scheme [13], wherein a pseudo time term is added to the dynamic equations and the physical time term is integrated by a second-order backward time discretization scheme and the pseudo time term is finally eliminated by a sub-iteration process. With the implementation of FVM for solid mechanics and dynamics in this work, the numerical methods can explicitly enforce the conservation laws in integral forms both locally and globally, whereas the traditional FEM can only do it globally. And unlike other FV methods, the cell-vertex FV method in this work does not use shape functions for spatial discretization. In addition, it is a matrix-free implicit dual-time stepping scheme, which can reduce computational efforts and storage requirements. And both static and dynamic solutions can be obtained with the same time-stepping method. To our knowledge, this work is the first ever attempt in using the dual time stepping scheme for structural dynamic problems. The successful implementation of FV method makes it possible to embed the FV structural dynamics solvers into exiting FV fluid dynamics solvers for solving fluid-structure interaction problems in a consistent manner, which reduces programming efforts greatly and improves computational efficiency.

2 Numerical methods

2.1 Governing equations

The governing equation for continuum undergoing motion is given by the Cauchy's equation in three dimensions:

$$\rho \boldsymbol{a} = \boldsymbol{b} + \nabla \bullet \boldsymbol{\sigma}_{ij} \tag{2.1}$$

Where $\boldsymbol{b}$ is body force, $\boldsymbol{\sigma}_{ij}$ the stress tensor, ρ the material density and $\boldsymbol{a}$ the acceleration. In this work, the term equation of dynamic equilibrium is adopted to distinguish it from static structural problems. For structures considered here, the body forces are negligible compared with stresses and other forces acting on them. There two types of these forces: the damping and external forces. External forces generally vary as functions of time. Damping is the ability of a structure to dissipate energy. In structural mechanics, the most common damping device is the ideal linear viscous damper. For a structure with linear viscous damping, the damping is directly proportional to the structure velocity, while acting in the opposite direction of the velocity. Discarding the body forces and considering the influences of external and damping forces, equation (2.1) is transformed into the following:

$$\rho \frac{\partial \boldsymbol{V}}{\partial t} = \nabla \bullet \boldsymbol{\sigma}_{ij} + \boldsymbol{f}(t) - c\boldsymbol{V} \tag{2.2}$$

and

$$\boldsymbol{V} = \begin{bmatrix} u \\ v \\ w \end{bmatrix}, \quad \boldsymbol{\sigma}_{ij} = \begin{bmatrix} \sigma_{xx} & \tau_{xy} & \tau_{xz} \\ \tau_{yx} & \sigma_{yy} & \tau_{yz} \\ \tau_{zx} & \tau_{zy} & \sigma_{zz} \end{bmatrix} \tag{2.3}$$

where $\boldsymbol{f}$ is the external force, $\boldsymbol{V}$ is the structure velocity,

c is damping ratio. The above equations are non-dimensionalized as

$$(x', y', z') = \left(\frac{x}{D}, \frac{y}{D}, \frac{z}{D}\right)$$
$$(u', v', w') = \left(\frac{u}{U_{\text{ref}}}, \frac{v}{U_{\text{ref}}}, \frac{w}{U_{\text{ref}}}\right);$$
$$t' = \frac{t}{D/U_{\text{ref}}}; \quad \boldsymbol{f}' = \frac{\boldsymbol{f}}{\rho(U_{\text{ref}})^2}; \quad \sigma'_{ij} = \frac{\sigma_{ij}}{\rho(U_{\text{ref}})^2}; \tag{2.4}$$

where D is the characteristic length of the structure, U_{ref} is reference velocity. Dropping the primes for simplicity, the non-dimensional governing equation is written as

$$\frac{\partial \boldsymbol{V}}{\partial t} = \nabla \bullet \boldsymbol{\sigma}_{ij} + \boldsymbol{f}(t) - \frac{D}{\rho U_{\text{ref}}} c\boldsymbol{V} \tag{2.5}$$

Equation (2.5) can be written as

$$\frac{\partial \boldsymbol{V}}{\partial t} = \nabla \bullet \boldsymbol{\sigma}_{ij} + \nabla \bullet \boldsymbol{F}(t) \tag{2.6}$$

where

$$\nabla \bullet \boldsymbol{F}(t) = \boldsymbol{f}(t) - \frac{D}{\rho U_{\text{ref}}} c\boldsymbol{V}$$

To adopt the finite volume scheme for structural analysis, the governing Eq. (2.6) is transformed into intergral form:

$$\frac{\partial}{\partial t} \iiint_{\text{cv}} \boldsymbol{V} \mathrm{d}V = \iiint_{\text{cv}} \nabla \bullet \boldsymbol{\sigma}_{ij} \mathrm{d}V + \int_{S_{\text{cv}}} \boldsymbol{F}(t) \bullet \mathrm{d}S \tag{2.7}$$

According to Green's theorem

$$\iiint_{\text{cv}} \nabla \bullet \boldsymbol{\sigma}_{ij} \mathrm{d}V = \oint_{S_{\text{cv}}} \boldsymbol{\sigma}_{ij} \cdot \boldsymbol{n} \, \mathrm{d}S \tag{2.8}$$

Finally, the integral governing equation (2.7) can be written as

$$\frac{\partial}{\partial t} \iiint_{\text{cv}} \boldsymbol{V} \mathrm{d}V = \oint_{S_{\text{cv}}} \boldsymbol{\sigma}_{ij} \cdot \boldsymbol{n} \, \mathrm{d}S + \oint_{S_{\text{cv}}} \boldsymbol{F}(t) \, \mathrm{d}S \tag{2.9}$$

2.2 Constitutive relationship

The constitutive relationship between stress and strain is the generalized Hook's law. For an isotropic homogeneous structure, it is given as

$$\begin{pmatrix} \sigma_{xx} \\ \sigma_{yy} \\ \sigma_{zz} \\ \tau_{xy} \\ \tau_{yz} \\ \tau_{xz} \end{pmatrix} = \frac{E}{(1+\upsilon)(1-2\upsilon)} \times \begin{bmatrix} 1-\upsilon & \upsilon & \upsilon & 0 & 0 & 0 \\ \upsilon & 1-\upsilon & \upsilon & 0 & 0 & 0 \\ \upsilon & \upsilon & 1-\upsilon & 0 & 0 & 0 \\ 0 & 0 & 0 & 1-2\upsilon & 0 & 0 \\ 0 & 0 & 0 & 0 & 1-2\upsilon & 0 \\ 0 & 0 & 0 & 0 & 0 & 1-2\upsilon \end{bmatrix} \times \begin{pmatrix} \varepsilon_{xx} \\ \varepsilon_{yy} \\ \varepsilon_{zz} \\ \gamma_{xy} \\ \gamma_{yz} \\ \gamma_{xz} \end{pmatrix} \tag{2.10}$$

where E is Young's Modulus, and ν is Poisson's ratio of the structure. The stress vector is $\boldsymbol{\sigma}^T = \begin{bmatrix} \sigma_{xx} & \sigma_{yy} & \sigma_{zz} & \tau_{xy} & \tau_{yz} & \tau_{xz} \end{bmatrix}$ and the strain vector is $\boldsymbol{\varepsilon}^T = \begin{bmatrix} \varepsilon_{xx} & \varepsilon_{yy} & \varepsilon_{zz} & \gamma_{xy} & \gamma_{yz} & \gamma_{xz} \end{bmatrix}$. The elastic strain can also be expressed in terms of total and initial strains as:

$$\boldsymbol{\sigma} = D(\varepsilon^t - \varepsilon^0) \tag{2.11}$$

where D is the constitutive matrix as shown in the large brackets in equation (2.10), $\boldsymbol{\varepsilon}^t$ and $\boldsymbol{\varepsilon}^0$are the total and initial strains respectively.

In this work, the strain–displacement formulation is expressed in the Green–Lagrange tensor as

$$\varepsilon_{ij} = \frac{1}{2}\left(\frac{\partial(\Delta X)_i}{\partial X_j} + \frac{\partial(\Delta X)_j}{\partial X_i} + \frac{\partial(\boldsymbol{\Delta X})}{\partial X_i} \bullet \frac{\partial(\boldsymbol{\Delta X})}{\partial X_i}\right) \tag{2.12}$$

where $\Delta \boldsymbol{X}^T = \begin{bmatrix} d_x & d_y & d_z \end{bmatrix}$ is the displacement vector. In vector form, the Green-Lagrange tensor can also be expressed as:

$$\begin{pmatrix} \varepsilon_{xx} \\ \varepsilon_{yy} \\ \varepsilon_{zz} \\ \gamma_{xy} \\ \gamma_{yz} \\ \gamma_{xz} \end{pmatrix} = \begin{pmatrix} \frac{\partial d_x}{\partial x} \\ \frac{\partial d_y}{\partial y} \\ \frac{\partial d_z}{\partial z} \\ \frac{1}{2}\left[\frac{\partial d_x}{\partial y} + \frac{\partial d_y}{\partial x} + \left(\frac{\partial d_x}{\partial x}\right)^2 + \left(\frac{\partial d_y}{\partial x}\right)^2 + \left(\frac{\partial d_z}{\partial x}\right)^2\right] \\ \frac{1}{2}\left[\frac{\partial d_y}{\partial z} + \frac{\partial d_z}{\partial y} + \left(\frac{\partial d_x}{\partial y}\right)^2 + \left(\frac{\partial d_y}{\partial y}\right)^2 + \left(\frac{\partial d_z}{\partial y}\right)^2\right] \\ \frac{1}{2}\left[\frac{\partial d_x}{\partial z} + \frac{\partial d_z}{\partial x} + \left(\frac{\partial d_x}{\partial z}\right)^2 + \left(\frac{\partial d_y}{\partial z}\right)^2 + \left(\frac{\partial d_z}{\partial z}\right)^2\right] \end{pmatrix} \tag{2.13}$$

2.3 Finite volume formulation

In this method, unstructured meshes are used to discretize the structural domain. Triangular and tetrahedral meshes are chosen for 2D and 3D cases respectively. Here the finite volume formulation is only described for 3D problems, bear in mind that it is straightforward to reduce it to a 2D formulation. The governing Eq. (2.7) is discretized on over tetrahedral cells as shown in Fig. 1. For every vertex, a control volume is constructed using the median dual of the tetrahedral mesh [14]. In Fig. 1, nodes A, P, B and C form the vertex of the tetrahedral cell and O is the center of cell APBC. Points a, b and c are the median duals of the edges AP, BP and CP respectively, while points 1, 2 and 3 are the centroids of triangles APC, CBP and ABP. In the cell-vertex scheme, the computed variables are stored at vertices A, P, B and C. Triangles APC, CBP, ABC and ABP form the corresponding control volume surfaces for the computation of strains, stresses and forces. The external force and stress terms in Eq. (2.7) for node P are calculated as

$$\iiint_{\mathrm{cv}} \nabla \bullet \boldsymbol{\sigma}_{ij} \mathrm{d}V = \oint_{S_{\mathrm{cv}}} \boldsymbol{\sigma}_{ij} \cdot \boldsymbol{n}\, \mathrm{d}S = \sum_{n=1}^{\mathrm{ncell}} \left[\sigma_{ij} \cdot \Delta S_c\right]_n \quad (2.14)$$

$$\oint_{S_{\mathrm{cv}}} \boldsymbol{F}(t)\, \mathrm{d}S = \sum_{n=1}^{\mathrm{ncell}} \left[f(t) \Delta S_c\right]_n \quad (2.15)$$

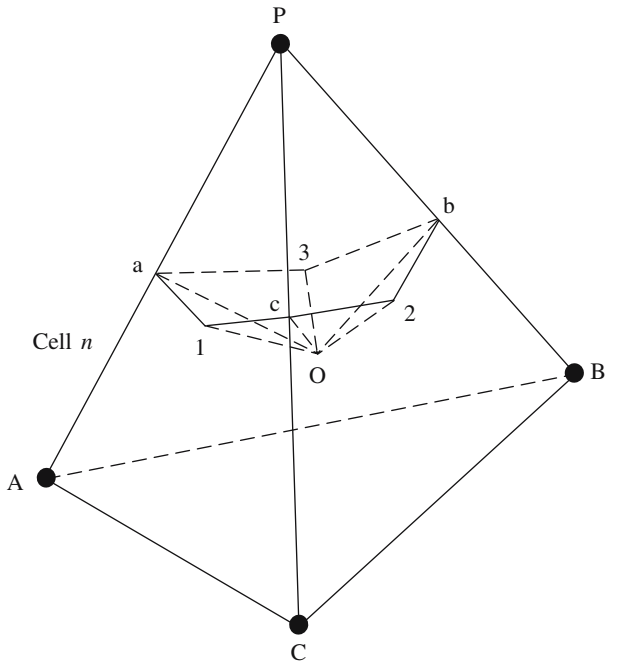

Fig. 1 Construction of control volume within a tetrahedron for a node P

where ncell is the number of elements associated with node P and ΔS_{cn} is the part of control volume surface in cell n. By using the following relation:

$$\oint_s \mathrm{d}S = 0 \quad (2.16)$$

The total vector surface of the control volume in a cell n becomes

$$\Delta S_{cn} = \frac{1}{3} \Delta S_{pn} \quad (2.17)$$

Thus, the computations of external force and stress can be simplified as

$$\oint_{S_{\mathrm{cv}}} \boldsymbol{\sigma}_{ij} \cdot \boldsymbol{n}\, \mathrm{d}S = \sum_{n=1}^{\mathrm{ncell}} \left[\sigma_{ij} \cdot \Delta S_c\right]_n = \frac{1}{3} \sum_{n=1}^{\mathrm{ncell}} \left(\sigma_{ij} \cdot \Delta S_p\right)_n \quad (2.18)$$

$$\oint_{S_{\mathrm{cv}}} \boldsymbol{F}(t)\, \mathrm{d}S = \sum_{n=1}^{\mathrm{ncell}} \left[f(t) \Delta S_c\right]_n = \frac{1}{3} \sum_{n=1}^{\mathrm{ncell}} \left(f(t) \Delta S_p\right)_n \quad (2.19)$$

where ΔS_{pn} is the surface vector of the face opposite node P of the tetrahedron under consideration.

The strain tensor ε_{ij} is calculated at the center of the tetrahedron with a node P, and can be obtained by using Green's Theorem based on the displacement vectors at the four vertices of the tetrahedron. Similar to the Galerkin type of formulation, the gradient of displacement vector ΔX at the center of a tetrahedron is evaluated as follows:

$$\begin{aligned} \mathrm{grad}(\Delta \boldsymbol{X}) &= -\frac{\sum_{k=1}^{4} (\Delta \boldsymbol{X})_k \cdot 9 S_k}{27 V} \\ &= -\frac{1}{3} \frac{\sum_{k=1}^{4} (\Delta \boldsymbol{X})_k \cdot S_k}{V} \end{aligned} \quad (2.20)$$

where $(\Delta \boldsymbol{X})_k$ is the displacement vector at a vertex k of the tetrahedron and S_k is the surface vector that is opposite to vertex k, V is the volume of the tetrahedron. The gradients of displacements obtained are substituted into Eq. (2.13) for the computations of strain tensor ε_{ij}. With the strain tensor, the stresses are calculated according to Eq. (2.10), and then the stresses are integrated over each control volume as specified by Eq. (2.18). The treatment of external forces is simpler since they are known functions. The integration of external forces is carried out over control volumes following Eq. (2.19).

2.4 Temporal discretization and integration

To enhance computational efficiency, an implicit dual time-stepping scheme, which is widely used for solutions of unsteady flows in CFD [13,15–17], is adopted in this work for time discretization. Implicit schemes

usually permit larger time-step sizes than explicit schemes, if not taking into consideration of accuracy.

Following Jameson's work [17], the derivative with respect to a fictitious pseudo time τ, is added to Eq. (2.7). Re-writing Eqs. (2.7) for a given node P with inputs from Eq. (2.18) and (2.19) and the pseudo-time term, the spatially discretized equations form a system of ordinary differential equations, which can be reformulated as

$$\begin{aligned}&\frac{\partial}{\partial\tau}(\boldsymbol{V}_p\Delta V_{\mathrm{cv}})\\&=-\left[\frac{\partial}{\partial t}(\boldsymbol{V}_p\Delta V_{cv})-\frac{1}{3}\sum_{n=1}^{\mathrm{ncell}}\left(\sigma_{ij}\cdot\Delta S_p\right)_n\right.\\&\qquad\left.-\frac{1}{3}\sum_{n=1}^{\mathrm{ncell}}\left(f(t)\Delta S_p\right)_n\right]\\&=-R(\boldsymbol{V}_p)\end{aligned}\tag{2.21}$$

where $R(\boldsymbol{V}_p)$ represents the residual, which includes stresses, external forces and inertial forces, ΔV_{cv} is the control volume of node P. The physical time derivative term $\frac{\partial}{\partial t}$ is discretized with a second-order accurate backward difference scheme, and the residual $R(\boldsymbol{V}_p)$ is reformulated as follows:

$$\begin{aligned}R(\boldsymbol{V}_p^{t+1})=&\frac{1.5\boldsymbol{V}_p^{t+1}\,\Delta V_{\mathrm{cv}}^{t+1}-2.0\,\boldsymbol{V}_p^{t}\Delta V_{\mathrm{cv}}^{t}+0.5\boldsymbol{V}_p^{t-1}\Delta V_{\mathrm{cv}}^{t-1}}{\Delta t}\\&-\frac{1}{3}\sum_{n=1}^{\mathrm{ncell}}\left(\sigma_{ij}\cdot\Delta S_p\right)_n-\frac{1}{3}\sum_{n=1}^{\mathrm{ncell}}\left(f(t)\Delta S_p\right)_n\end{aligned}\tag{2.22}$$

The superscript $(t+1)$ denotes the time level $(t+1)$ Δt and all the variables are evaluated at this time level. Thus Eq. (2.21) can be written in the following discrete form:

$$\frac{\mathrm{d}\boldsymbol{V}_p^{t+1,m}}{\mathrm{d}\tau}\Delta V_{\mathrm{cv}}^{t+1}=-R(\boldsymbol{V}_p^{t+1,m})\tag{2.23}$$

whose solution is sought by marching to a pseudo equilibrium state in τ. Here m denotes the pseudo time level $m\Delta\tau$. Once the artificial equilibrium state is reached, the derivative of $\boldsymbol{V}_p$ with respect to τ becomes zero, and the solution satisfies $R(\boldsymbol{V}_p^{n+1})=0$. This is actually the solution of Eq. (2.7). Hence, the original governing equation is fully recovered. Therefore, instead of solving the governing equation at each time step in physical time domain (t), the problem is transformed into a sequence of pseudo equilibrium-state computations in the artificial time domain (τ). This can be performed using a pseudo time explicit five-stage Runge–Kutta scheme [18, 19]. For time integration, Eq. (2.23) is re-formulated as

$$\frac{\boldsymbol{V}_p^{t+1,m+1}-\boldsymbol{V}_p^{t+1,m}}{\Delta\tau}\Delta V_{\mathrm{cv}}^{t+1}=-R(\boldsymbol{V}_p^{t+1,m})\tag{2.24}$$

To advance the solution in pseudo time from m to $m+1$, the formulation of a five-stage Runge–Kutta scheme is adopted:

$$\begin{aligned}\boldsymbol{V}_p^{(0)}&=\boldsymbol{V}_p^{m}\\\boldsymbol{V}_p^{(1)}&=\boldsymbol{V}_p^{(0)}-\alpha_1\frac{\Delta\tau}{\Delta V_{\mathrm{cv}}}R(\boldsymbol{V}_p^{(0)})\\\boldsymbol{V}_p^{(2)}&=\boldsymbol{V}_p^{(0)}-\alpha_2\frac{\Delta\tau}{\Delta V_{\mathrm{cv}}}R(\boldsymbol{V}_p^{(1)})\\\boldsymbol{V}_p^{(3)}&=\boldsymbol{V}_p^{(0)}-\alpha_3\frac{\Delta\tau}{\Delta V_{\mathrm{cv}}^{(2)}}R(\boldsymbol{V}_p^{(2)})\\\boldsymbol{V}_p^{(4)}&=\boldsymbol{V}_p^{(0)}-\alpha_4\frac{\Delta\tau}{\Delta V_{\mathrm{cv}}}R(\boldsymbol{V}_p^{(3)})\\\boldsymbol{V}_p^{(5)}&=\boldsymbol{V}_p^{(0)}-\alpha_5\frac{\Delta\tau}{\Delta V_{\mathrm{cv}}}R(\boldsymbol{V}_p^{(4)})\\\boldsymbol{V}_p^{(m+1)}&=V_p^{(5)}\end{aligned}\tag{2.25}$$

where the stage coefficients for a five-stage Runge–Kutta time integration are as follows:

$$\alpha_1=\frac{1}{4},\quad\alpha_2=\frac{1}{6},\quad\alpha_3=\frac{3}{8},\quad\alpha_4=\frac{1}{2},\quad\alpha_5=1$$

To improve convergence rates, residual smoothing [15] is adopted, which only destroys time accuracy in pseudo time without affecting the accuracy in physical time. The idea behind this is to replace the residual at one vertex with a smoothed or weighted average of the residuals at the neighboring vertices. The averaged residuals are calculated implicitly in order to increase the local pseudo time step size, thus increasing the convergence rate. The smoothing equation for a vertex k can be expressed as

$$\bar{R}_k=R_k+\varepsilon\,\bar{R}_k\tag{2.26}$$

where R is the original residual, $\bar{R}$ is smoothed residual and ε is the smoothing coefficient, which can be defined as

$$\varepsilon=\max\left\{\frac{1}{4}\left[\left(\frac{\mathrm{CFL}}{\mathrm{CFL}^*}\right)^2-1\right],0\right\}\tag{2.27}$$

where CFL^* is the maximum CFL number of the basic scheme. The solution to the above equations can be obtained on an unstructured grid by using Jacobi iterative method as follows:

$$\bar{R}_k^{(m)}=R_k^{(0)}+\varepsilon\sum_{i=1}^{\mathrm{numnod}(k)}[\bar{R}_i^{(m)}-\bar{R}_k^{(m)}]$$

i.e.

$$\bar{R}_k^{(m)}=\frac{R_k^{(0)}+\varepsilon\sum_{i=1}^{\mathrm{numnod}(k)}\bar{R}_i^{(m-1,m)}}{1+\varepsilon\cdot\mathrm{numnod}(k)}\tag{2.28}$$

where numnod(k) is the number of neighboring nodes of vertex k. After the velocity is obtained, the displacement is calculated using the average of $\boldsymbol{V}^{t-1}$ and $\boldsymbol{V}^{t}$ as

$$(\Delta \boldsymbol{X})^{t+1} = (\Delta \boldsymbol{X})^{t} + \frac{\Delta t}{2}\left(\boldsymbol{V}^{t+1} + \boldsymbol{V}^{t}\right) \tag{2.29}$$

2.5 Lumped mass representation and dynamic behavior of structures

This work aims to compute the structural dynamics where the presence of inertial force in Eq. (2.7) is represented by lumped mass matrix. In numerical analysis, there are two different types of representations for discrete mass, i.e., the lumped mass matrix and the consistent mass matrix. For FE methods, both representations are possible depending on the models analyzed. However for the cell-vertex FV formulation described in this work, the lumped mass matrix is the only possible choice for the FV stress and strain analyses.

The natural frequency of a structure depends on its material properties, geometry and the loading conditions acting on it. A structure may exhibit extensional, torsional, flexural deformation or a combination of all three. If a structure is subject to a combination of extensional and flexural deformations the resulting natural frequencies will differ from those occurring in pure flexure or pure extension. The natural frequencies for flexural modes of vibration are of most interest since the natural frequencies are significantly lower than those for extensional or torsional deformation, which may result in higher stresses in the structure [20]. Axial loads applied to slender structures may be extensile or compressive. Tensile loads will increase the natural frequency of a structure while the compressive loads will decrease them, while concentrated transverse loads and body forces will always decrease the natural frequency [20].

2.6 Boundary conditions

The boundary conditions used in this work include fully clamped and simply supported boundary conditions. For simply supported edges, the following conditions are imposed:

(a) $\Delta \boldsymbol{X} = 0$, no displacement on the edge;
(b) $\nabla(\Delta \boldsymbol{X}) \neq 0$, rotation of the edge is allowed;
(c) $\boldsymbol{Q} \neq 0$, shear forces are prescribed on the edge;
(d) $\boldsymbol{M} = 0$, bending moments are zero.

For fully clamped edges, the following conditions are applied:

(a) $\Delta \boldsymbol{X} = 0$, no displacement occurs on the edge;
(b) $\nabla(\Delta \boldsymbol{X}) = 0$, rotation of the edge is suppressed;
(c) $\boldsymbol{Q} \neq 0$, shear forces are prescribed;
(d) $\boldsymbol{M} \neq 0$, bending moments are prescribed.

3 Numerical results and discussions

3.1 Deformation and dynamics of a 2D cantilever

The solver is first tested on a 2D clamped-free cantilever supporting a load at its free end [21], a benchmark case in structural mechanics. The cantilever is illustrated in Fig. 2, where h, d and l are the height, width and length of the cantilever respectively. F is the imposed load and for 2D analysis it is assumed that d=1.0. The static solution to this problem given by Timoshenko and Goodier [21] allows a slight distortion at the free end of the cantilever, whereas the solution given by Fenner [22] has no such distortions. This test case requires no such displacement or distortion at the free end of the cantilever, therefore the y displacement at the free end given by Fenner [22] is adopted:

$$d_y = -\frac{4Fl^3}{Edh^3} \tag{3.1}$$

where E is Young's modulus. The load F imposed at the free end is set to be 250 N. The static solution given in Eq. (3.1) is independent of Poisson's ratio and is applicable to a cantilever undergoing pure bending, i.e. no axial load is applied and out of plane load on the cantilever is zero. Thus for comparison with the analytical solution a zero Poisson's ratio is assumed. The geometrical and material parameters of this cantilever are tabulated in Table 1.

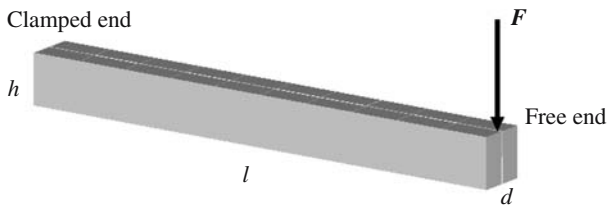

Fig. 2 A clamped-free end cantilever

Table 1 Geometry and material properties for a 2D cantilever

Geometry		Material properties	
Length l	20.0 m	Young's modulus E	10 MPa
Width d	1.0 m	Density ρ	2, 600 Kg/m^3
Height h	2.0 m	Load F	250 N

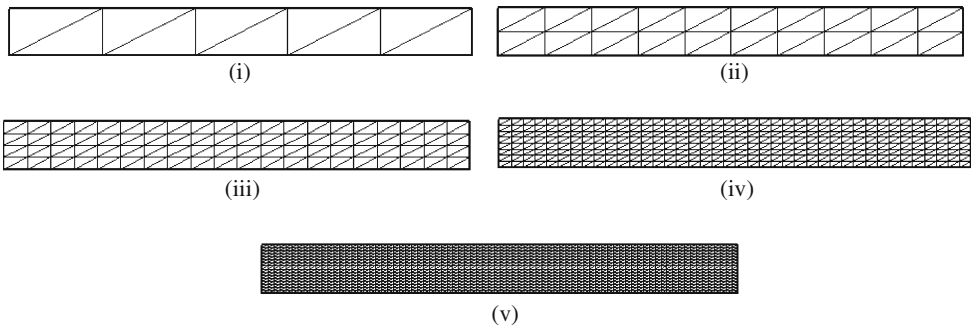

Fig. 3 Grids used for Grid convergence study; (*i*) 5 × 2 elements; (*ii*) 10 × 4 elements; (*iii*) 20 × 8 elements; (*iv*) 40 × 16 elements; (*v*) 80 × 16 elements

With the above parameters and the load applied, Eq. (3.1) gives the static displacement at the tip of the cantilever is −0.1 m. Before embarking on the dynamic analysis of the 2D cantilever, a grid-independent solution to the static displacement problem is sought. Five grids are studied for the cantilever displacement as shown in Fig. 3:

1. Grid (i) 5×2 elements, 12 grid nodes;
2. Grid (ii) 10×4 elements, 33 grid nodes;
3. Grid (iii) 20×8 elements, 105 grid nodes;
4. Grid (iv) 40×16 elements, 369 grid nodes;
5. Grid (v) 80×16 elements, 1,377 grid nodes.

The percentage errors in the *y* displacement are illustrated in Fig. 4 and tabulated in Table 2. A percentage error of 4.2% is found with grid (iv) and a percentage error of 1.5% is observed with grid (v). Thus grid (iv) is deemed to fine enough, which is chosen for further analysis. All simulations were run on an Origin Graphic 2000 workstation. And with the chosen grid (iv), the CPU time is about 15 min.

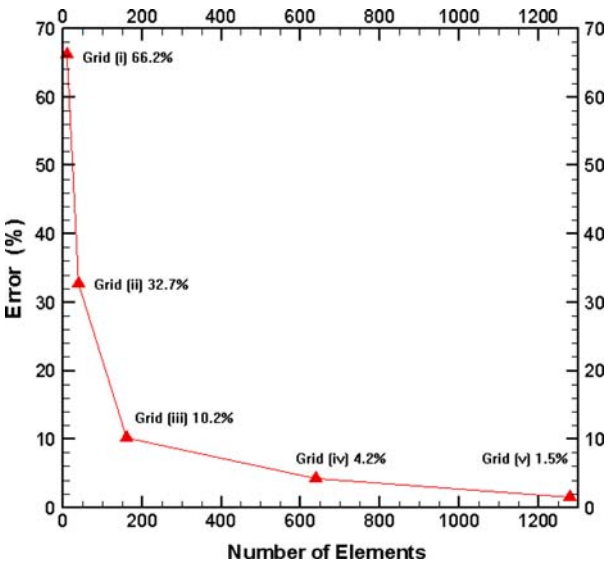

Fig. 4 Grid convergence study for 2D cantilever

Table 2 Grids and percentage errors for 2D cantilever

Grids	Percentage errors (%)
(i) 5×2 elements	66.2
(ii) 10×4 elements	32.7
(iii) 20×8 elements	10.2
(iv) 40×16 elements	4.2
(v) 80×16 elements	1.5

The maximum bending stress at the root of the cantilever occurs at the upper surface [23], which is calculated as follows:

$$(\sigma_{xx})_{\max} = \frac{My}{I_z} = \frac{6FL}{dh^2} \tag{3.2}$$

With the 250 N load, the maximum bending stress at the root of the cantilever is 7,500 Pa. The distributions of bending (σ_{xx}) and shear (τ_{xy}) stress obtained on grid (iv) are presented in Figs. 5 and 6. In the calculated results, the bending stress on the upper surface at the root of cantilever registers a value of 7,360 Pa, about 1.8% deviation from the analytical result of 7,500 Pa. The distribution of shear stress in the cantilever distributes has a parabolic shape along the transverse direction, with a maximum shear stress at the center and zero values on the upper and lower surfaces [23]. The maximum shear stress is calculated as

$$(\tau_{xy})_{\max} = -\frac{Fh^2}{8I_z} = -\frac{3}{2}\frac{F}{dh} \tag{3.3}$$

The maximum shear stress at the center is −1, 800 Pa in the simulated result, which agrees with the analytical solution of −1, 875 Pa calculated by Eq. (3.3).

The dynamic responses of the cantilever are investigated in two different cases: forced vibration and free vibration. The forced vibration is the dynamic response of the cantilever under the imposed load *F*. The cantilever starts vibrating once the load is applied and it will finallyreach a steady state with its steady-state

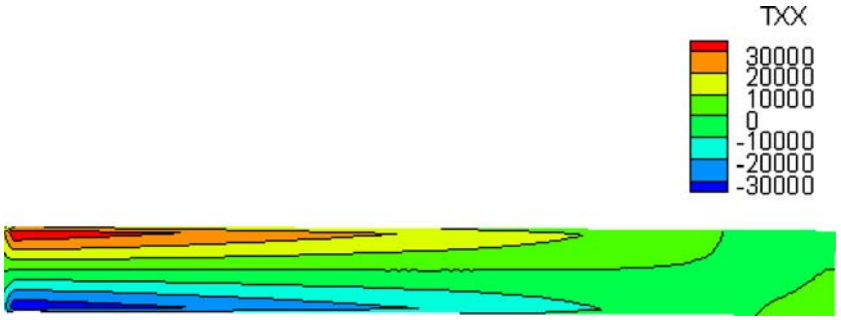

Fig. 5 Distribution of bending stress σ_{xx}(Pa)

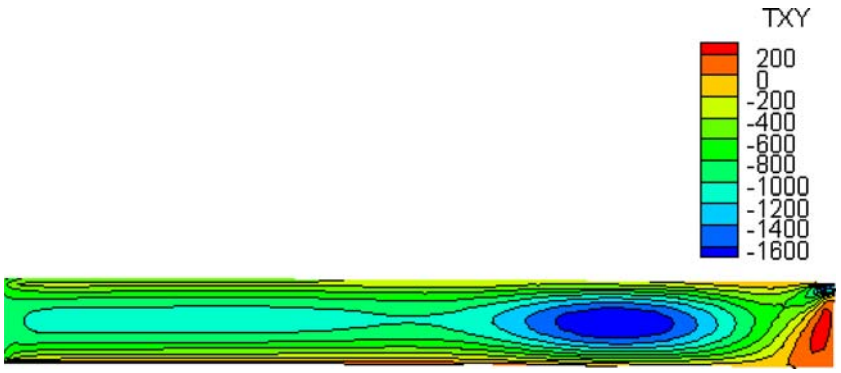

Fig. 6 Distribution of shear stress τ_{xy}(Pa)

displacement. The forced vibration of the cantilever under constant load F [24] can be described as the following:

$$y(t) = \left(y_0 - \frac{F}{k}\right)\mathrm{e}^{-\varsigma\omega_n t}\cos\omega_d t + \left[\frac{\varsigma\omega_n(y_0 - F/k) + \dot{y}_0}{\omega_n\sqrt{1-\varsigma^2}}\right]\mathrm{e}^{-\varsigma\omega_n t}\sin\omega_d t - \frac{F}{k} \quad (3.4)$$

$$\dot{y}(t) = \dot{y}_0\mathrm{e}^{-\varsigma\omega_n t}\cos\omega_d t - \left[\frac{\omega_n(y_0 - F/k) + \varsigma\dot{y}_0}{\sqrt{1-\varsigma^2}}\right]\mathrm{e}^{-\varsigma\omega_n t}\sin\omega_d t \quad (3.5)$$

where $y(t)$, $\dot{y}(t), y_0$ and $\dot{y}_0$ are the displacement, velocity, initial displacement and initial velocity of the tip of the cantilever respectively, $\omega_n$and ω_d are undamped and damped natural frequencies of the cantilever. $\varsigma = \frac{c}{2m\omega_n}$ is critical damping ratio, which represents damping in the structure. In this work, a 10% damping ratio is adopted. $k = \frac{3EI}{l^3}$ is the stiffness of the structure. The undamped natural frequency [24] for the first mode of vibration of the cantilever is

$$\omega_n = (1.875)^2\sqrt{\frac{EI_z}{ml^4}} \quad (3.6)$$

and the damped natural frequency [24] is

$$\omega_d = \omega_n\sqrt{1-\varsigma^2} \quad (3.7)$$

The steady-state response is obtained from Eqs. (3.4) and (3.5) by taking the limit as $t \to \infty$. Since $e^{-\varsigma\omega_n t} \to 0$ as $t \to \infty$, it follows that

$$y_{\mathrm{ss}} = -\frac{F}{k} = -\frac{F}{3EI_z/l^3} = -\frac{4Fl^3}{Edh^3} \quad (3.8)$$

$$\dot{y}_{\mathrm{ss}} = 0 \quad (3.9)$$

Equation (3.8) is actually the same as Eq. (3.1), which calculates the maximum displacement at the tip. The velocity of the cantilever in forced vibration finally decreases to zero as stated in Eq. (3.9).

Free vibration of the cantilever is initiated by releasing the load on the cantilever after reaching its steady status, with an initial displacement of y_{ss} and a zero initial velocity. The equation describing free vibration [24] is

$$\frac{y(t)}{y_{\mathrm{ss}}} = \mathrm{e}^{-\varsigma\omega_n t}\left[\cos\omega_d t + \left(\frac{\varsigma}{\sqrt{1-\varsigma^2}}\right)\sin\omega_d t\right] \quad (3.10)$$

The displacement history of free vibration is shown in Fig. 7, in which the simulated frequency and period are found to be 0.053 Hz and 19 s. They compare favorably with the analytical frequency and period of 0.05 Hz and 20 s.

3.2 Deformation and dynamics of a 3D cantilever

The 2D cantilever studied in the previous section is extended to three dimensions as shown in Fig. 2. For the

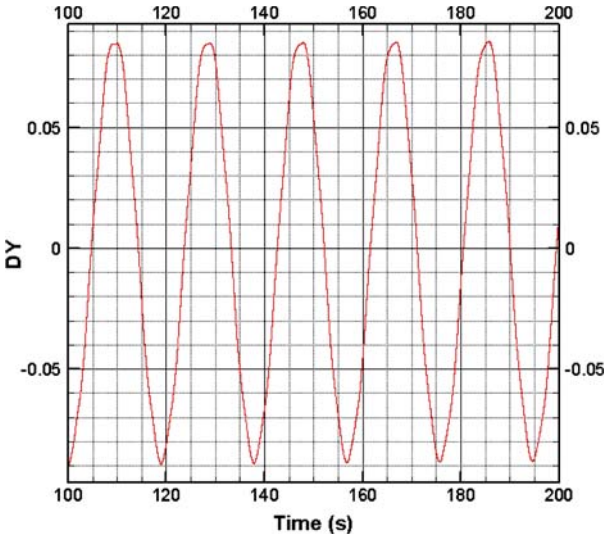

Fig. 7 Displacement history of free vibration of 2D cantilever

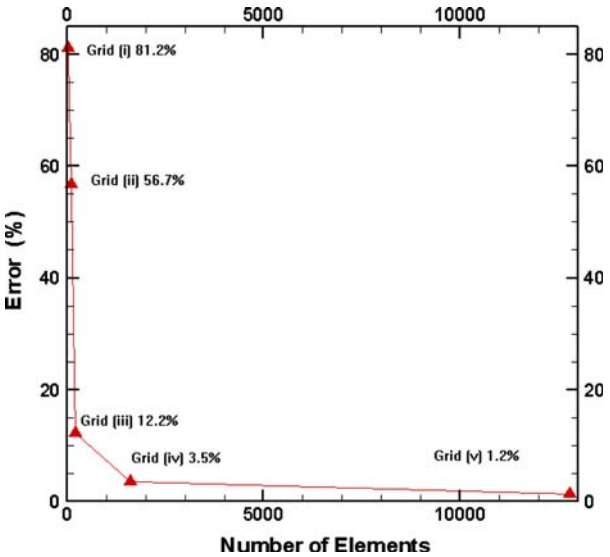

Fig. 8 Grid convergence study for 3D cantilever

Table 3 Grids and percentage errors for 3D cantilever

Grids	Percentage errors (%)
(i) 25 elements	81.2
(ii) 100 elements	56.7
(iii) 200 elements	12.2
(iv) 1,600 elements	3.5
(v) 12,800 elements	1.2

3D case, the depth of the cantilever is 2 m. Length and width remain the same. The imposed load increases to 500 N. Material properties are the same as the 2D cantilever as listed in Table 1. With these geometrical and material parameters, displacement at the tip of cantilever is −0.1 m according to Eq. (3.1). A grid convergence study is also performed for the 3D cantilever on five consecutively finer grids, which are listed as follows:

(a) grid (i) 5×5×1 25 elements, 24 grid nodes;
(b) grid (ii) 5×5×4 100 elements, 54 grid nodes;
(c) grid (iii) 10×5×4 200 elements, 99 grid nodes;
(d) grid (iv) 20×5×8 1,600 elements, 525 grid nodes;
(e) grid (v) 40×20×16 12,800 elements, 3,321 grid nodes.

The results of the grid convergence study are tabulated in Table 3 and illustrated in Figure 8. It is found that grid (iv) is fine enough for the 3D cantilever. On the Origin Graphic 2000 workstation, the CPU time for the simulation is about 30 min.

The distributions of σ_{xx} and τ_{xz} at mid-y plane of the loaded cantilever are shown in Figs. 9 and 10. The maximum bending stress σ_{xx} is 7,500 Pa according to Eq. (3.2). It is observed that the numerical results agree well with the analytical solutions. The time history of displacement for free vibration of the cantilever is shown in Fig. 11. The period of free vibration of the 3D cantilever is 13.8 s as found in Fig. 11, which is in accordance with the analytical value of 14 s.

3.3 Simply-supported square plate

The third test case is a simply-supported square plate subject to a uniformly distributed load as shown in Fig. 12. The geometry of the plate is 20 × 20 × 0.5 m. A mesh of 40 × 40 × 10 elements is chosen for the simulation after a grid convergence investigation. Young's modulus E and Poisson's ratio ν of the plate are 10 MPa and 0.3. The density of the plate is 2,600 kg/m^3 . And the uniform load q is 10 N/m^2 . The maximum displacement occurs at the center of the plate in z direction, and the analytical solution of the maximum displacement given by Timoshenko [25] is

$$W_{\max} = -0.00406\frac{qL^4}{D} \tag{3.11}$$

where

$$D = \frac{Et^3}{12(1-\nu^2)} \tag{3.12}$$

and L is the length of edge and t is the thickness of the plate. Therefore $W_{\max}$ is −0.057 m according to Eq. (3.11). The displacement contour of the plate is shown in Fig. 13, in which the maximum displacement occurs at the center with a value of −0.054 m, a small deviation from the analytical solution. The maximum bending stresses $(\sigma_{xx})_{\max}$ and $(\sigma_{yy})_{\max}$ are at the center of the plate [25].

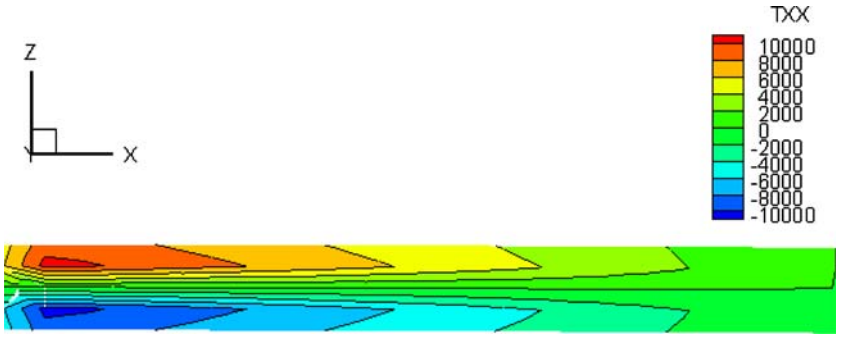

Fig. 9 Distribution of bending stress σ_{xx} on the mid-y plane

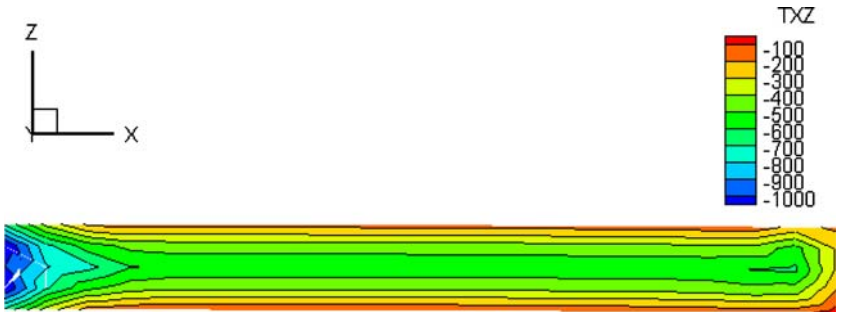

Fig. 10 Distribution of shear stress τ_{xz} on the mid-y plane

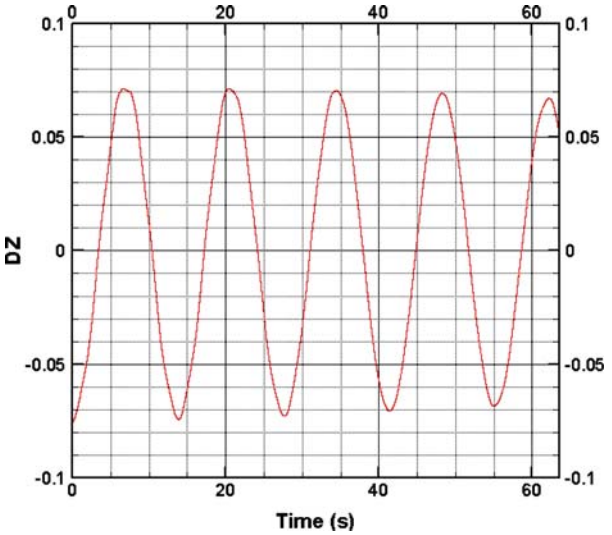

Fig. 11 Displacement history of free vibration of 3D cantilever

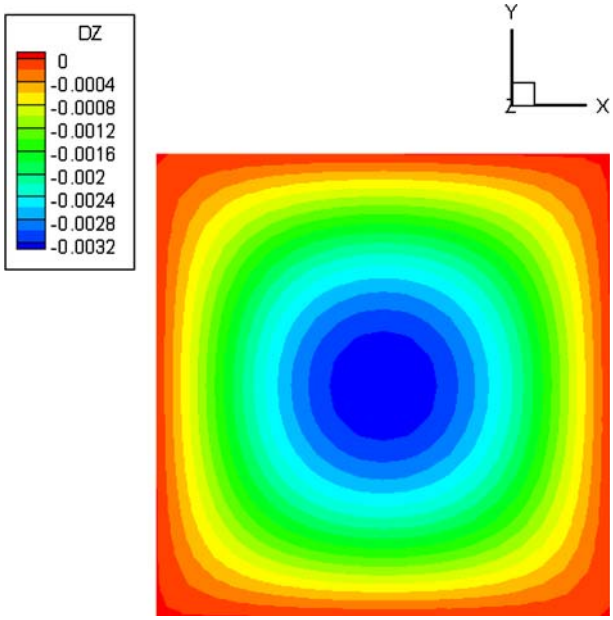

Fig. 13 Displacement contours of a simply-supported square plate

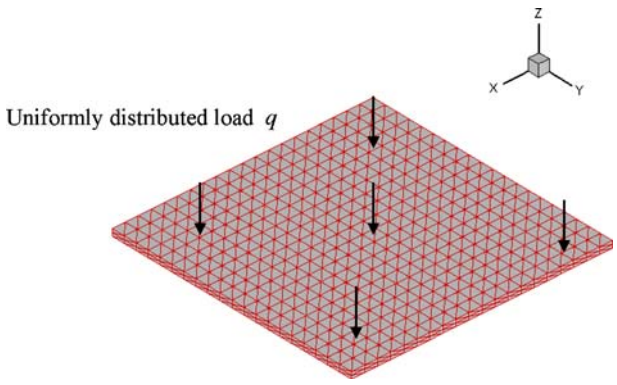

Fig. 12 Geometry and mesh of a square plate

For a square plate, $(\sigma_{xx})_{\max}$ is equal to $(\sigma_{yy})_{\max}$, which is calculated as

$$(\sigma_{xx})_{\max} = (\sigma_{yy})_{\max} = -\frac{3qL^2(1+\nu)}{2\pi t^2} \tag{3.13}$$

Maximum shear stresses $(\tau_{xz})_{\max}$ and $(\tau_{yz})_{\max}$ occur at the middle of the edges of plate [25]. They are calculated as follows:

$$(\tau_{xz})_{\max} = (\tau_{yz})_{\max} = -\frac{3qL(3-\nu)}{8\pi t} \tag{3.14}$$

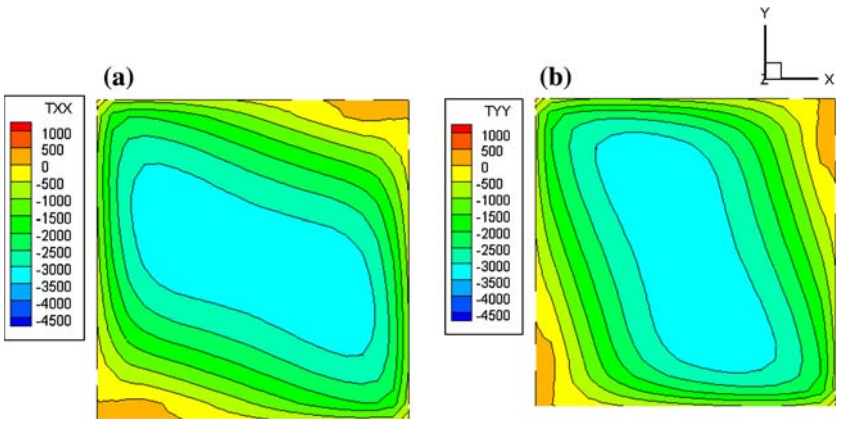

Fig. 14 **a** Distribution of σ_{xx}; **b** Distribution of σ_{yy} on the upper surface of plate

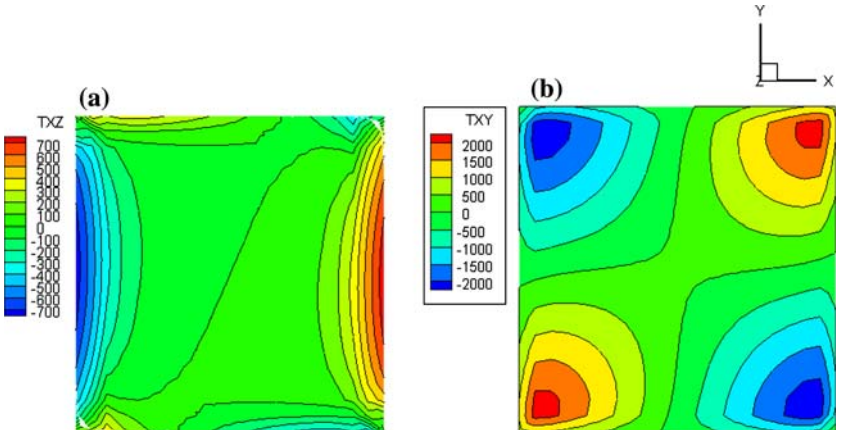

Fig. 15 **a** Distribution of τ_{xz} on the mid-it z plane; **b** Distribution of τ_{xy}

Hence the analytical values of maximum bending and shear stresses are $-3,164$ Pa and -129 Pa respectively. The distributions of bending stresses and shear stresses are presented in Figs. 14 and 15. In Fig. 14, it is found that $(\sigma_{xx})_{\max}$ and $(\sigma_{yy})_{\max}$ are $-3,208$ Pa at the center. And in Fig. 15(a), the maximum shear stress $(\tau_{xz})_{\max}$ is at the middle of edges along y direction of the plate, with a value of -150 Pa. The distribution of τ_{yz} is in the same pattern as τ_{xz}, except the maximum value occurs at the center of the edge along x direction. The distribution of τ_{xy} is also presented in Fig. 15(b). Compared with the analytical values, it is observed that the numerical results are in good agreement with the analytical solutions obtained from Eqs. (3.13) and (3.14).

The imposed load is released after the plate reaches its steady state, the dynamic response is investigated for free vibration of the plate with an initial displacement. The frequency parameter of the free vibration is calculated as [26]

$$\lambda^2 = \frac{\omega^2 L^4 m}{D} = \left(2\pi^2\right)^2 \tag{3.15}$$

hence

$$\omega = \frac{2\pi^2}{L}\sqrt{\frac{D}{m}} \tag{3.16}$$

Therefore the exact frequency of free vibration of the plate is 0.4639 rad/s and the period is 2.2 s. The free vibration of the plate is presented in Fig. 16, in which the displacement is recorded at the center of plate. It is observed in the numerical result that the period of free vibration is 2.1 s and the frequency is 0.476 rad/s. The simulation for the simply-supported square plate takes about 60 min in CPU time.

3.4 Clamped square plate

In this section, the square plate studied in the last section is modified with clamped boundaries, whilst all other parameters remain the same. The maximum displacement occurs at the center of plate [25], which is given as

$$W_{\max} = -0.00126\frac{qL^4}{D} \tag{3.17}$$

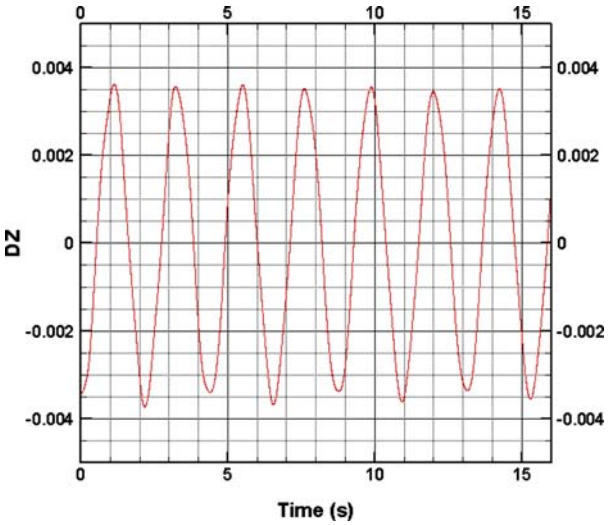

Fig. 16 Displacement history of free vibration of the simply supported plate

which generates a maximum displacement of −0.0176 m. The numerical result gives a maximum displacement at the center of −0.019 m as shown in Fig. 17. The maximum bending moment occurs at the middle of the edges [25] which is calculated by

$$M_{\max} = 0.0513qL^2 \tag{3.18}$$

Therefore the maximum bending stresses at the middle of the edges are

$$(\sigma_{xx})_{\max} = (\sigma_{yy})_{\max} = \frac{6M_{\max}}{t^2} \tag{3.19}$$

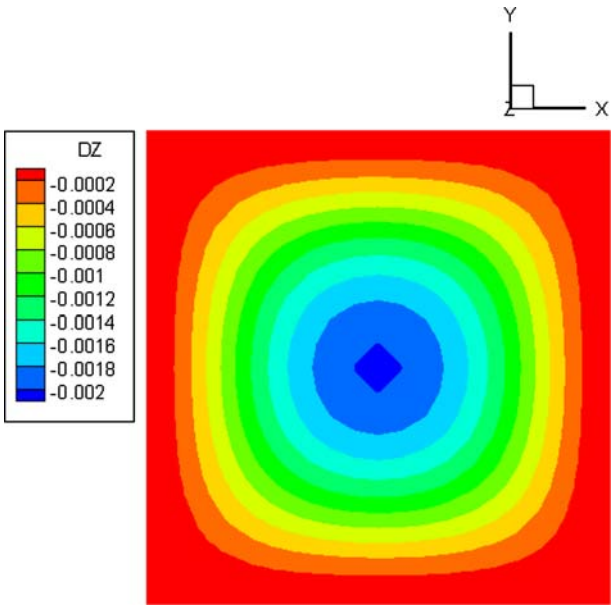

Fig. 17 Displacement contours of a fully clamped square plate

Hence the analytical value of maximum bending stresses is 2,462 Pa. The simulated distributions of bending stresses σ_{xx} and σ_{yy} are presented in Fig. 18. It is found in this Figure that the maximum bending stresses are at the middle of the edges with a value of 2,500 Pa, which agree well with the analytical values. The maximum shear stresses also occur at the middle of edges of the plate, which are calculated as [25]

$$(\tau_{xz})_{\max} = \frac{1}{2}(\sigma_{xx} - \sigma_{zz}) \tag{3.20}$$

$$(\tau_{yz})_{\max} = \frac{1}{2}(\sigma_{yy} - \sigma_{zz}) \tag{3.21}$$

The analytical solution obtained from Eq. (3.17) is 2,400 Pa. $(\tau_{xz})_{\max}$ occurs at the middle of the edge along y and $(\tau_{yz})_{\max}$ occurs at the middle of the edge along x as found in the simulation results, which are presented in Fig. 19(a). The distribution of τ_{xy} is also presented in Fig. 19(b). From the above analysis, it can be concluded that the numerical results agree well with the analytical solutions in terms of displacements and stress distributions.

The dynamic response of the clamped plate is studied for free vibration, which is initiated from the deformed status after it is released from the uniformly distributed load. The frequency parameter given by Leissa [26] is

$$\lambda^2 = \frac{\omega^2 L^4 m}{D} = (35.6852)^2 \tag{3.22}$$

hence

$$\omega = \frac{35.6852}{L}\sqrt{\frac{D}{m}} \tag{3.23}$$

which shows that the exact frequency of free vibration of the plate is 0.8386 rad/s and the period is 1.2 s. The free vibration of the clamped plate is presented in Fig. 20, in which the displacement is recorded at the center of plate. It is observed in the numerical result that the period of free vibration is 1.26 s . The CPU time for the simulation of the clamped square plate is almost the same as that of the simply-supported square plate.

4 Conclusions

A new 3D vertex-centered unstructured-grid finite volume scheme is proposed in this work for structural static and dynamic analysis. Stresses are evaluated using the Green Theorem based on grid cells. To obtain time accurate dynamic solutions, implicit dual time stepping scheme is employed. Local timestepping scheme and

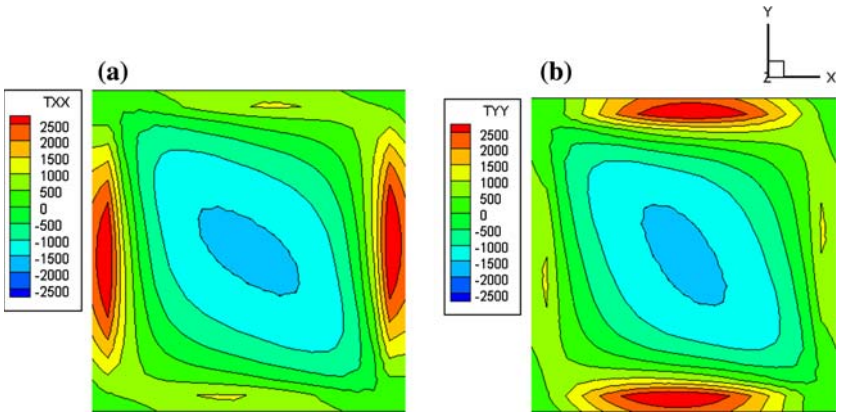

Fig. 18 **a** Distribution of σ_{xx}; **b** Distribution of σ_{yy} on the upper surface of plate

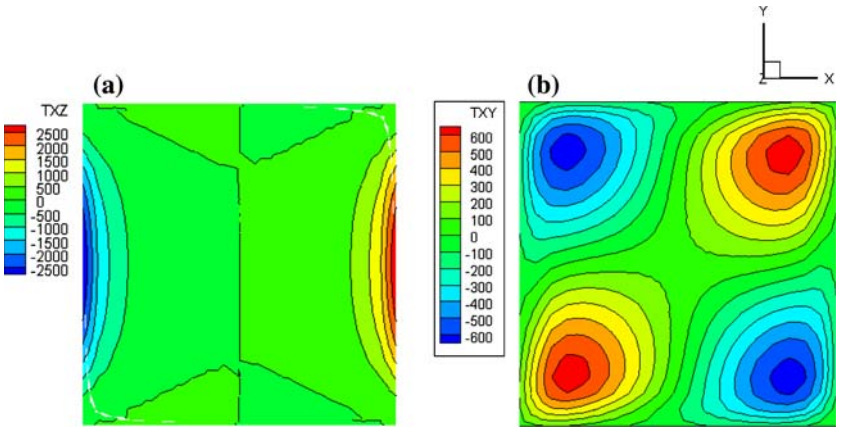

Fig. 19 **a** Distribution of τ_{xz} on the mid-z plane; **b** Distribution of τ_{xy}

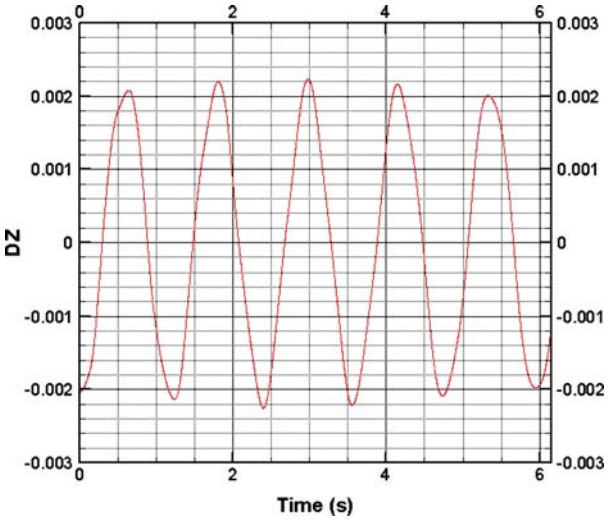

Fig. 20 Displacement history of free vibration of the fully clamped plate

residual smoothing in pseudo time are implemented to improve convergence. Numerical experiments prove that the method is accurate and efficient in the analysis of structural deformation and dynamics.

Acknowledgements The authors would like to acknowledge the research fund provided by Biomedical Research Council (BMRC) of Agency for Science, Technology and Research (ASTAR) of Singapore.

References

1. Onate E, Cevera M, Zienkiewicz OC (1994) A finite volume method format for structural mechanics. Int J Numerical Methods Eng 37:181–201
2. Idelsohn SR, Onate E (1994) Finite volumes and finite elements: two 'Good Friends'. Int J Numerical Methods Eng 37:3323–3341
3. Demirdzic I, Muzaferija S, Peric M (1997) Benchmark solutions of some structural analysis problems using finite volume method and multigrid acceleration. Int J Numerical Methods Eng 40:1893–1908
4. Wheel MA (1997) A finite volume method for analysing the bending deformation of thick and thin plates. Comput Methods Appl Mech Eng 147:199–208
5. Fallah N (2004) A cell vertex and cell centered finite volume method for plate bending analysis. Comput Methods Appl Mech Eng 193:3457–3470
6. Demirdzic I, Muzaferija S, Peric M (1994) Finite volume method for stress analysis in complex domains. Int J Numerical Methods Eng 37:3751–3766

7. Bailey C, Cross M (1995) A finite volume procedure to solve elastic solid mechanics problems in three dimensions on an unstructured mesh. Int J Numerical Methods Eng 38:1756–1776
8. Demirdzic I, Martinovic D (1993) Finite volume method for thermo-elasto plastic stress analysis. Comput Methods Appl Mech Eng 109:331–349
9. Slone AK, Bailey C, Cross M (2003) Dynamic solid mechanics using finite volume methods. Appl Math Model 27:69–87
10. Slone AK, Pericleous K, Bailey C, Cross M, Bennet C (2004) A finite volume unstructured mesh approach to dynamic fluid-structure interaction: an assessment of the challenge of predicting the onset of flutter. Appl Math Model 28:211–239
11. Wheel MA (1996) Geometrically versatile finite volume formulation for plane strain elastostatic stress analysis. J Strain Anal Eng Des 31:111–116
12. Taylor GA, Bailey C, Cross M (2003) A vertex-based finite volume method applied to non-linear material problems in computational solid mechanics. Int J Numerical Methods Eng 56:507–529
13. Xia GH, Zhao Y, Yeo JH (2005) Numerical simulation of 3D fluid-structure interaction using an immersed membrane method. Mod Phys Lett 19:28–29
14. Zhao Y, Tai CH (2001) Higher-order characteristics-based methods for incompressible flow computation on unstructured grids. AIAA J 39(7):1280–1287
15. Zhao Y, Zhang BL, Tan CH (2002) A high-resolution characteristics-based implicit dual time stepping VOF method for free surface flow simulation on unstructured grids. J Comput Phys 183
16. Tai CH, Zhao Y, Liew KM (2005) An unstructured parallel-multigrid matrix-free implicit method for computation of unsteady incompressible viscous flows using a high-resolution characteristics-based scheme. Comput Methods Appl Mech Eng 194:36–38
17. Jameson A (1991) Time dependent calculations using multigrid, with applications to unsteady flows past airfoils and wings. AIAA Paper 91–1596, June 1991
18. Rogers SE, Kwak D, Kiris C (1991) Steady and unsteady solutions of the incompressible Navier-Stokes equations. AIAA J 29(4):603–610
19. Pedley TJ, Stephanoff KD (1985) Flow along a channel with a time-dependent indentation in one wall: the generation of vorticity waves. J Fluid Mech 160:337–367
20. Schiff D (1990) Dynamic analysis and failure modes of simple structure. Wiley, New York
21. Timoshenko SP, Goodier JN (1982) Theory of Elasticity. McGraw-Hill, New York
22. Fenner RT (1986) Engineering elasticity: applications of numerical and analytical techniques. Ellis Horwood, New York
23. Timoshenko SP (1972) Mechanics of materials. Brooks/Cole Engineering Division, Monterey
24. Hart GC, Wong K (1999) Structural dynamics for structural engineers. Wiley, New York
25. Timoshenko SP, Wienowsky-Kreiger S (1959) Theory of plates and shells, 2nd edn. McGraw-Hill, New York
26. Leissa AW (1973) The free vibration of rectangular plates. J Sound Vib 31(3):257–293